Physical Modeling of Process-Machine-Interactions in Micro Machining

Andreas Lange[1]
Institute for Manufacturing Technology and Production Systems,
Technische Universität Kaiserslautern, Germany

Benjamin Kirsch
Institute for Manufacturing Technology and Production Systems,
Technische Universität Kaiserslautern, Germany

Marius Heintz
Institute for Manufacturing Technology and Production Systems,
Technische Universität Kaiserslautern, Germany

Jan C. Aurich
Institute for Manufacturing Technology and Production Systems,
Technische Universität Kaiserslautern, Germany

Abstract

Increasing demands for smaller and smarter devices in a variety of applications requires the investigation of process-machine-interactions in micro manufacturing to ensure process results that guarantee part functionality. One approach is the use of simulation-based physical models. In this contribution, methods for the physical modeling of high-precision air bearing and magnetic bearing spindles are presented in addition to a kinematic model of the micro milling process. Both models are superimposed in order to carry out investigations of the slot bottom surface roughness in micro end milling. The results show that process-machine-interactions in micro manufacturing can be modeled by the superposition of a physical model of the machine tool spindle taking cutting forces into consideration and a purely kinematic model of the machining process, providing the necessary tools for a variety of further investigations into process-machine-interactions in micro manufacturing.

2012 ACM Subject Classification Applied computing → Physical sciences and engineering

Keywords and phrases multiphysics, air bearing, magnetic bearing, surface roughness modeling, micro milling

Digital Object Identifier 10.4230/OASIcs.iPMVM.2020.2

Funding *Andreas Lange*: This research was funded by the Deutsche Forschungsgemeinschaft (DFG, German Research Foundation) – 252408385 – IRTG 2057.

1 Introduction

The increasing demand for smaller and smarter products in a wide range of applications poses new challenges for manufacturing technology [31]. Even the slightest influence on the machining process, whether machine or process induced, can harm the functionality of the component [7]. For this reason, the investigation of process-machine-interactions is moving into focus within the field of micro cutting [1]. The term process-machine-interaction (PMI) refers to the interaction between a manufacturing process and the machine tool used. These interactions can negatively influence the machining process and thus need to be investigated in order to minimize potentially harmful process-machine-interactions and also identify possible positive effects of certain process-machine-interactions on process results [8]. In

[1] Corresponding author

2nd International Conference of the DFG International Research Training Group 2057 – Physical Modeling for Virtual Manufacturing (iPMVM 2020).
Editors: Christoph Garth, Jan C. Aurich, Barbara Linke, Ralf Müller, Bahram Ravani, Gunther Weber, and Benjamin Kirsch; Article No. 2; pp. 2:1–2:20

OpenAccess Series in Informatics
Schloss Dagstuhl – Leibniz-Zentrum für Informatik, Dagstuhl Publishing, Germany

macro machining, numerous methods to analyze the effects of process-machine-interactions have been developed. A comprehensive overview of these methods can be found in [7] and [8]. Process-machine-interactions can affect both the machine tool, especially the machine tool spindle and the tool, and the process result. This can result in increased tool wear or premature tool breakage [8]. Also, process-machine-interactions can influence the process result and thus eventually affect the functionality of the part [13]. In micro machining, the dimensions of the tool and the chip to be removed are significantly smaller than in macro machining, which causes changes in the physical behavior during machining known as size effects [27], which is why existing methods for investigating process-machine-interactions in macro manufacturing cannot be adopted to micro manufacturing [1]. As such, the machine tool and machine tool spindle, including the tool, must be regarded as separate aspects [21]. While macro machining aims to reduce chatter vibrations by increasing the stiffness of the machine tool and using shorter or stiffer tools, an excessive influence of spindle run-out on the process result is observed in micro machining [21]. Thus, in order to use simulation-based physical models to investigate process-machine-interactions in micro manufacturing, detailed physical models of both the machine tool spindle including the tool, and the process, are required to capture process-machine-interactions.

Simulation-based investigations of micro cutting are either based on purely kinematic simulations [3, 23], chip formation simulations [2], or on kinematic simulations with added cutting force models [1, 22, 26]. Purely kinematic simulations model the ideal process kinematics and thus allow a determination of the shape of the chip to be removed, the slot geometry, and the ideal surface roughness in the slot bottom and slot flank [21]. However, these purely kinematic simulations do not consider the influence of machine vibrations and cutting forces and thus do not allow an investigation of process-machine-interactions [3, 23]. Chip formation simulations can be used to analyze the cutting energies, cutting forces and chip geometry under consideration of the cutting tool geometry and elasticity and plasticity effects of the workpiece material [2]. The difficulty lies in the need for a precise knowledge of the workpiece‘s elastic and plastic behavior [20]. Additionally, chip formation simulations require a high amount of computing time and resources [2]. Because of this requirement, usually only a fraction of the tool movement is modeled [25, 20], preventing the investigation process-machine-interactions. Kinematic simulations with added cutting force models are able to combine the advantages of purely kinematic simulations without omitting the influence of the cutting forces. As such, coupling these models and the kinematics of the machine tool is a promising approach to model process-machine-interactions in micro manufacturing and has already been implemented by several researchers [1, 26, 15]. As of now, the implemented machine tool kinematics are based on beam models of the tool, allowing the consideration of tool deflection but do not include the vibrational behavior of the spindle.

Due to the excessive influence of the machine tool spindle's behavior on the process result in micro machining [21], high-precision spindles for micro manufacturing are required. Because of the high requirements in terms of low friction, precision, stiffness, damping, and rotational speeds, air bearings and magnetic bearings are used almost exclusively. Various physical models for the investigation of air bearings have been presented [29, 19]. Most of these models are based on the Reynolds equation for thin-film fluid flows [24]. This Reynolds equation assumes an inertialess, laminar fluid flow. However, the accuracy of air bearing simulations modeled with the Reynolds equation suffers from neglecting inertia effects, sophisticated turbulence models and the analytical approximation of the orifice inlet mass flow rate [11]. Magnetic bearings require a multiphysical simulation model to allow data exchange between the coupled structural-electromagnetic-closed-loop-behavior [17]. Usually,

the electromagnetic behavior is modeled using the magnetic circuit method, which represents the magnetic bearing through a network of resistors [17]. The magnetic circuit method is based on the electromagnetic force calculation of a simple U-shaped magnet and thus not able to fully capture the electromagnetic behavior of complex geometries and nonlinear material behavior [17]. Detailed finite element models can capture the spindle's rotordynamic behavior considering gyroscopic effects and mass unbalance [19, 12]. But these rotordynamic models of high-precision spindles usually do not include the influence of tool clamping, tool geometry, and cutting forces, meaning that process-machine-interactions cannot be analyzed with these models [12].

The benefit of investigating process-machine-interactions using physical simulation models is the ability to identify the influences and effects of single parameters on components and the overall process result [8]. Furthermore, simulations can be used to quantify parameters relevant for the understanding of process-machine-interactions, which are difficult or impossible to determine experimentally [25]. Thus, physical models can be a valuable resource to deepen the understanding of tool behavior, machine vibrations and process behavior considering the process-machine-interaction. However, for a proper simulation-based investigation into process-machine-interactions in micro cutting, the aforementioned shortcomings must be overcome to achieve the modeling accuracy required to capture process-machine-interaction influences and effects. The objective of this paper is to present a suitable method for modeling process-machine-interactions in micro manufacturing. For this purpose, methods for the accurate physical modeling of machine tool spindles supported by air bearings and magnetic bearings, as well as methods for the kinematic modeling of the process kinematics are given. Further, a method for the superposition of machine and process kinematics is given to enable the investigation of process-machine-interactions under consideration of cutting forces.

2 Methods

As explained in section 1, modeling process-machine-interactions in micro manufacturing requires high-quality simulation models, which are able to capture the small-scale phenomena of micro machining. This section describes the methods used to model the machine kinematics with emphasis on the machine tool spindle dynamics as well as the process kinematics of micro end milling.

2.1 Machine kinematics

The overall kinematic behavior of machine tool spindles is mainly influenced by the spindle's bearings, the rotor's dynamics due to structural loads, the rotor's dynamics due to thermal loads, the tool clamping, and the tool (see also [21]). This necessitates a physical model of the machine tool spindle which is able to capture all of the aforementioned aspects.

2.1.1 Air bearing spindles

The physical model of an air bearing spindle can be set up by first setting up, simulating, and evaluating the fluid dynamics model of the air bearings and then using the results of this fluid dynamics model for the structural dynamics model of the rotor, tool clamping, and tool. For this purpose, the relevant bearing characteristics to be determined are the dynamic stiffness and damping coefficients. These bearing characteristics can be evaluated using the small perturbation method [6]. Herein, five cases of the fluid dynamics model must be set up. The first case is used to determine the equilibrium pressure distribution

(and thus fluid forces acting on the rotor) under the bearing's given static load, such as gravitational force. Subsequently, the rotor, which is in its equilibrium position, is perturbed to obtain induced restoring forces and hence dynamic characteristics of the bearing. Since the induced forces are directly proportional to the displacements and associated velocities, only four additional cases are necessary to determine the perturbed pressure distributions: a perturbation along the x-direction (case 2), a perturbation along the y-direction (case 3), a perturbation along the x-direction with an applied perturbation velocity in x-direction (case 4), and a perturbation along the y-direction with an applied perturbation velocity in y-direction (case 5). Once all five pressure distributions are known, the dynamic stiffness and damping coefficients can be calculated.

ANSYS Fluent 2019R3 and ANSYS Mechanical APDL 2019R3 were used to set up the models and conduct the simulations [2].

Bearing characteristics

Since the majority of air bearing spindles are equipped with inlet restricted air bearings, where pressurized air is fed into the bearing gap through a discrete number of orifices, this paper will only focus on this air bearing configuration. Further, isotherm fluid flow may be assumed [29] and air is modeled by the ideal gas law.

A schematic view of an aerostatic journal bearing with a feed orifice is given in figure 1. The geometric properties are given by the rotor radius R, the orifice radius r_0, the bearing length L, and the bearing gap c. Pressurized air with a predefined pressure p is forced into the bearing gap through a restricting orifice. The air flows through the bearing gap and exists the bearing at the rear and front face of the bearing ($x = L$), where ambient pressure p_a prevails. Due to unavoidable external excitations and manufacturing errors, the centers of the rotor and the bearing sleeve are never coincident, but are offset by small deviations in x- and y-direction (Δx, Δy). Hence, the bearing gap height h is a sum of the coaxial bearing clearance c (bearing gap height for a rotor and bearing sleeve perfectly coincident with respect to each other) and the eccentricity e. Consequently, the bearing gap height varies with respect to the circumference of the rotor.

The fluid flow within the bearing can be divided into three regions:

- the orifice region (I),
- the entrance region (IIa)) and
- the gap region (IIb)).

Within the orifice and entrance region, the abrupt redirection of the air flow leads to complex flow phenomena such as turbulence and eddies [9]. In the gap region, these complex flow phenomena have already subsided, which leads to a viscous/laminar flow [29]. The corresponding qualitative pressure profile within an aerostatic journal bearing is depicted by the blue line in figure 1. A detailed representation of the pressure distribution, including the pressure drop in the entrance region (IIa) is required for the accurate computation of the rotors' equilibrium position, the equilibrium pressure distribution and hence for the computation of the static and dynamic characteristics.

For the solution of the equilibrium pressure distribution and with respect to the different behavior within the bearing regions I and II, the fluid dynamics model of an aerostatic journal bearing can be split up into two submodels, which are then coupled through an

[2] Naming of specific manufacturers is done solely for the sake of completeness and does not necessarily imply an endorsement of the named companies nor that the products are necessarily the best for the purpose.

iterative solution approach at the interface depicted in red in figure 1. The split up submodels are shown in figure 1. Even though both submodels must be solved during every iteration, dividing the aerostatic bearing into two submodels is computationally more efficient compared to the use of a single computational domain. This is due to the two submodels not requiring the meshing and computation of multiple three-dimensional orifice regions.

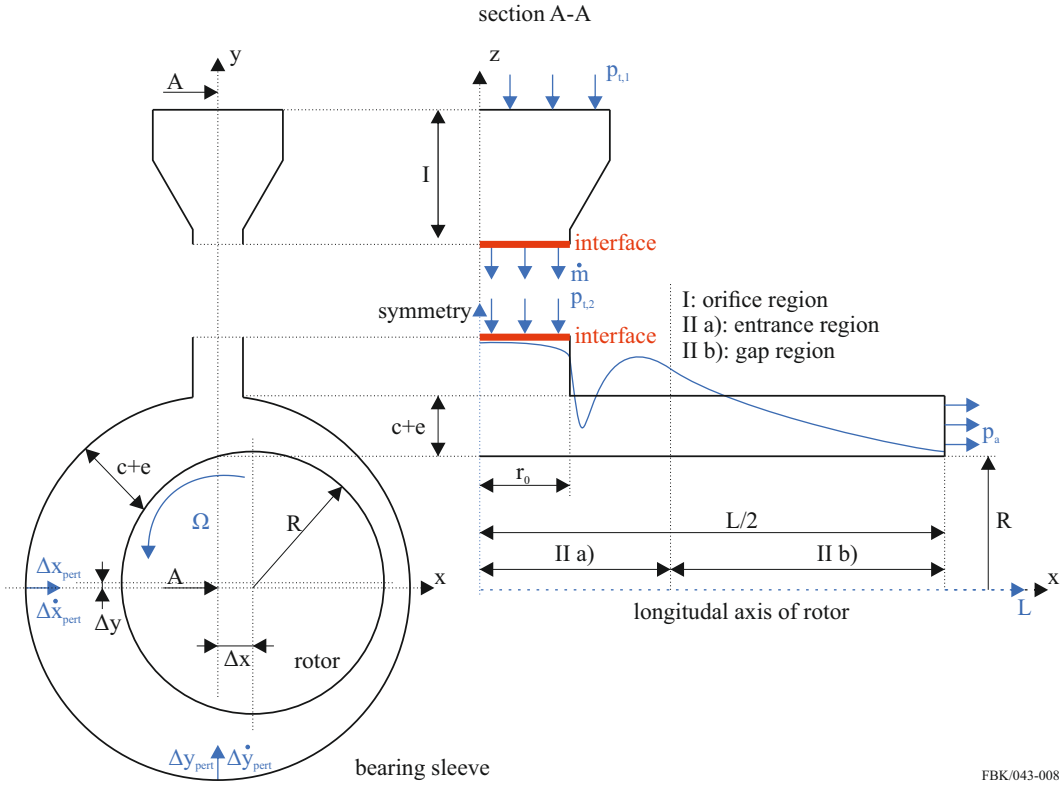

Figure 1 Schematic view of an aerostatic journal bearing with qualitative pressure profile in the individual regions.

Submodel I consists of the orifice region (I). Taking advantage of the symmetric geometry of the orifice, a two-dimensional simulation model can be set up by applying a rotational symmetry boundary condition to the orifice centerline. The boundary conditions of this submodel are specified by applying a predefined supply pressure $p_{t,1}$ at the orifice inlet and a mass flow rate $\dot{m}$ at the interface (the orifice region's outlet). The exact value of the mass flow rate is yet unknown. The governing equations for this submodel are the Reynolds-averaged Navier-Stokes equations for axisymmetric geometries [5]. Turbulence is modeled using the Menter-k-ω-SST model [30].

Submodel II consists of the entrance region (IIa)) and the gap region (IIb)). Because of the varying gap height, a three-dimensional simulation model is required and only one symmetry boundary condition can be applied at the y-z-plane. The boundary conditions of this submodel are specified by applying an interface pressure $p_{t,2}$ at the interface (entrance region's inlet). This interface pressure is dependent on the prior solution of submodel I and as such yet unknown. At the bearing outlet, an ambient pressure p_a is applied. The rotational speed boundary condition is applied to the rotor. The fluid flow in submodel II can be modeled using the Reynolds-averaged Navier-Stokes equations [5].

Using an iterative solution approach, both submodels can be coupled to determine the correct mass flow rate and interface pressure. In order to determine suitable initial conditions for the mass flow rate m_{init} and interface pressure, an analytical formula for the calculation of the mass flow rate through the orifice may be used. This formula is given by [28]:

$$\dot{m}_{init} = C_D \cdot 2\pi r_0 c \cdot \Psi \left(2 \cdot p_i \cdot \frac{p_i}{R_S T_{abs}} \right) \tag{1}$$

where C_D is the discharge coefficient [28], R_S is the specific gas constant, $T_{abs}$is the absolute temperature, and Ψ is the discharge function [28] of the fluid.

With the analytical formula, both submodels, and the defined interface boundary conditions, the following algorithm can be employed to determine the stationary pressure distribution in the bearing:

1. Analytical calculation of initial mass flow rate $\dot{m}_{init}$ value according to equation 1
2. Simulation of orifice region using determined mass flow rate
3. Determination of total pressure $p_{t,2}$ at orifice outlet
4. Simulation of entrance and gap regions using $p_{t,2}$ as the inlet boundary condition
5. Determination of mass flow rate $\dot{m}$ evaluated at entrance and gap regions
6. Repeat steps 2 to 5 until convergence criteria are met

For aerostatic bearings, suitable convergence criteria can be established by monitoring the scaled residuals of the Reynolds-averaged Navier-Stokes equations and the fluid forces acting on the rotor in x- and y-direction. Convergence can be assumed as soon as the fluid forces remain constant and the scaled residuals either drop by four orders of magnitude or remain constant. Convergence should not be judged by just monitoring the scaled residuals of Reynolds-averaged Navier-Stokes without monitoring the fluid forces.

Once the convergence criteria are met, the first of the aforementioned five cases is solved and the equilibrium pressure distribution is obtained. For the remaining four cases, the mass flow rate and pressure $p_{t,2}$ can be reused. Hence, only region II must be recomputed.

The remaining four cases are set up similar to the first case, the only difference being an additional boundary condition applied to the bearing sleeve to account for the perturbation defined by the perturbation increment. This boundary condition is applied as follows:

- case 2: an additional translational offset Δx_{pert} is applied to the bearing sleeve,
- case 3: an additional translational offset Δy_{pert} is applied to the bearing sleeve,
- case 4: an additional translational offset Δx_{pert} and a translational velocity $\Delta \dot{x}$ is applied to the bearing sleeve,
- case 5: an additional translational offset Δy_{pert} and a translational velocity $\Delta \dot{y}$ is applied to the bearing sleeve.

Once all five cases are solved, the pressure distributions can be integrated to obtain the fluid forces acting on the rotor. Using the small perturbation method, a first order Taylor series expansion yields:

$$F_{x,i} = F_{x,1} + k_{xx}\Delta x + k_{xy}\Delta y + c_{xx}\Delta \dot{x} + c_{xy}\Delta \dot{y}, \qquad i = 2,3,4,5 \tag{2}$$

$$F_{y,i} = F_{y,1} + k_{yx}\Delta x + k_{yy}\Delta y + c_{yx}\Delta \dot{x} + c_{yy}\Delta \dot{y}, \qquad i = 2,3,4,5 \tag{3}$$

It can be seen from equations 2 and that no additional case with superpositioned perturbations along both the x- and y-direction is necessary. For example, in case 2, a single perturbation along the x-direction gives a perturbation of zero in y-direction and zero perturbation velocity, which cancels out the cross-coupled stiffness term $k_{xy} \cdot \Delta y$ and the damping terms and hence enables the computation of the direct stiffness k_{xx}. The same principle holds for case 3. For case 4, a perturbation along the x-direction and the application of a perturbation

velocity $\Delta\dot{x}$ again cancels out the cross-coupled stiffness term $k_{xy} \cdot \Delta y$ and the damping term $c_{xy} \cdot \Delta y_{pert}$. Using the result of case 2, the direct stiffness k_{xx} is already known, and thus the direct damping c_{xx} can be computed. where k and c are called linearized stiffness and damping coefficients respectively. Once again, the same principle holds for case 5. Finally, the individual stiffness and damping coefficients can be computed as:

$$\begin{pmatrix} k_{xx} & k_{xy} \\ k_{yx} & k_{yy} \end{pmatrix} = \begin{pmatrix} \frac{F_{2,x}-F_{1,x}}{\Delta x} & \frac{F_{3,x}-F_{1,x}}{\Delta y} \\ \frac{F_{2,y}-F_{1,y}}{\Delta x} & \frac{F_{3,y}-F_{1,y}}{\Delta y} \end{pmatrix}, \qquad \begin{pmatrix} c_{xx} & c_{xy} \\ c_{yx} & c_{yy} \end{pmatrix} = \begin{pmatrix} \frac{F_{4,x}-F_{1,x}}{\Delta \dot{x}} & \frac{F_{5,x}-F_{1,x}}{\Delta \dot{y}} \\ \frac{F_{4,y}-F_{1,y}}{\Delta \dot{x}} & \frac{F_{5,y}-F_{1,y}}{\Delta \dot{y}} \end{pmatrix} \quad (4)$$

where the first index of Force F depicts the case number which the force is evaluated in and the second index depicts whether the force acts in x- or y-direction.

Rotordynamics

The general dynamic equation to describe a system in motion is given by [10]:

$$[\mathbf{M}]\left\{\ddot{U}\right\} + [\mathbf{C}]\left\{\dot{U}\right\} + [\mathbf{K}]\{U\} = f \quad (5)$$

where $\mathbf{M}$, $\mathbf{C}$ and $\mathbf{K}$ are the mass, damping and stiffness matrices, and f is the external force vector. In rotordynamics, this equation gets additional contributions from the gyroscopic effect [G], and the rotating damping effect [B] which leads to the modified equation [10]:

$$[\mathbf{M}]\left\{\ddot{U}\right\} + ([\mathbf{G}] + [\mathbf{C}])\left\{\dot{U}\right\} + ([\mathbf{B}] + [\mathbf{K}])\{U\} = f \quad (6)$$

Equation 6 is formulated using a stationary reference frame. The bearing coefficients, calculated with the methods in section 2.1.1 are incorporated in the matrices $\mathbf{K}$ and $\mathbf{C}$. The external force vector f contains the mass unbalance forces, cutting forces and may also include additional external forces, such as magnetic bearing forces (section 2.1.2).

2.1.2 Magnetic bearing spindles

The physical model of magnetic bearing spindles consists of the calculation of the electromagnetic forces and the setup of the rotordynamics model. For the required data exchange during the whole simulation, both aspects must be included in the closed loop model used for the control system analysis. In this section, a method is introduced, where the electromagnetic forces are first obtained using a three-dimensional electromagnetic finite element method (FEM) simulation model. These forces are then stored within lookup-tables to represent the behavior of a simulation model within the control loop.

Evaluation of electromagnetic forces

A schematic view and the applied boundary conditions of a radial heteropolar 4-pole-pair active magnetic bearing are shown in figure 2.

A pole configuration of alternating north (N) and south (S) poles (depicted by the N and S symbols in two of the eight poles in figure 2a)) and a differential winding scheme is employed. Herein, one electromagnet is operated with the sum of the bias current i_0 and the control current i while the opposite electromagnet uses the difference (figure 2b)). This ensures that the current and thus the force increase in one electromagnet to the same extent as they decrease in the other electromagnet. Depending on the material used, both the rotor and the iron core can exhibit magnetic saturation, where an increase of the applied external magnetic field H does not significantly increase the magnetic flux density B within

the material [17]. Regarding the magnetic bearing shown in figure 2, this means that once the material is saturated, an increase of the currents through the coils does only lead to a neglectable change in the electromagnetic forces. This nonlinear behavior is included in the model through so-called B-H-curves [17]. The required boundary conditions for the three-dimensional electromagnetic simulation are the number of turns, the conducting area, the current flow direction and the current value for every coil. An edge-based magnetic vector potential method based on the Maxwell equations [14], is used for the solution and evaluation of the magnetic flux distribution and magnetic forces. The electromagnetic simulation model computes electromagnetic forces based on predefined current inputs. However, the magnetic forces also depend on the rotor position. Hence, the model must be parametric regarding the rotor's position in x- and y-direction to fully capture the dependencies $f_{mag,x} = f(x, y, i_x, i_y)$ and $f_{mag,y} = f(x, y, i_x, i_y)$ to generate accurate lookup-tables.

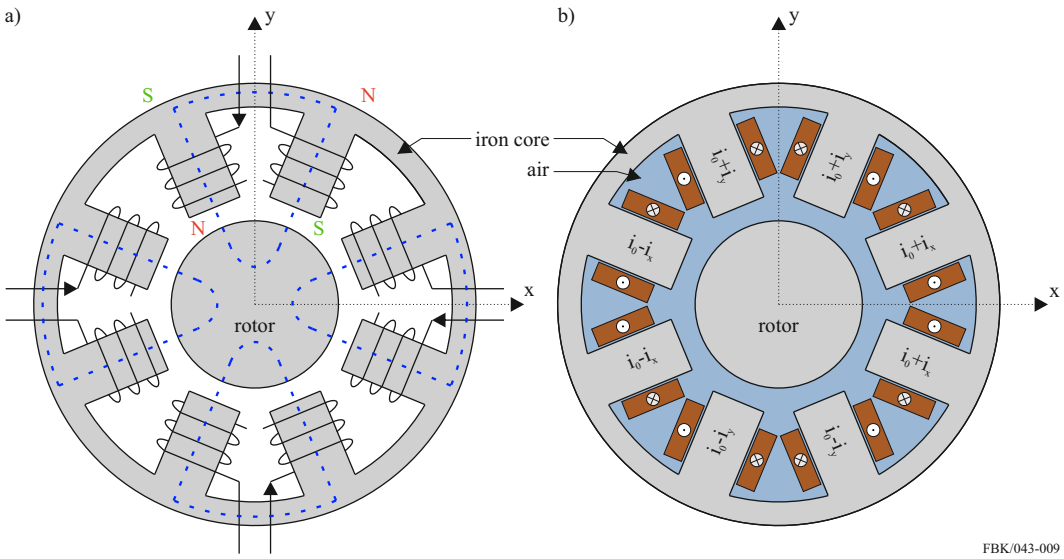

Figure 2 a) schematic view and b) boundary conditions of a radial heteropolar 4-pole-pair active magnetic bearing.

Rotordynamics

The magnetic bearing spindle's rotordynamics can be described using either equation 5 or equation 6. Compared to the rotordynamics of the air bearing spindle, where the bearing characteristics are inserted into the left-hand-side of the dynamics equation, in the rotordynamics model of the magnetic bearing spindle the bearing forces are applied as additional external forces within the force vector f, acting on the rotor.

Control system

Simulink R2019b [3] is used for the setup of the control system model. Distributed proportional-integral-derivative (PID) control is used for the current control of the magnetic bearing.

[3] Naming of specific manufacturers is done solely for the sake of completeness and does not necessarily imply an endorsement of the named companies nor that the products are necessarily the best for the purpose.

Herein, each controlled variable (currents i_x, i_y) is assigned an input (positions x, y). A single-variable PID controller is designed and implemented for each pair of inputs and outputs. Implementing independent PID controllers for the current control in both x- and y-direction, the dynamics equations (equation 5 or 6), and the magnetic bearing characteristics through the described lookup-tables, one obtains a model of the closed loop, which can be used for the system simulation and the controller design. The closed loop can be seen in figure 3a), with a detailed schematic of the plant given in figure 3b).

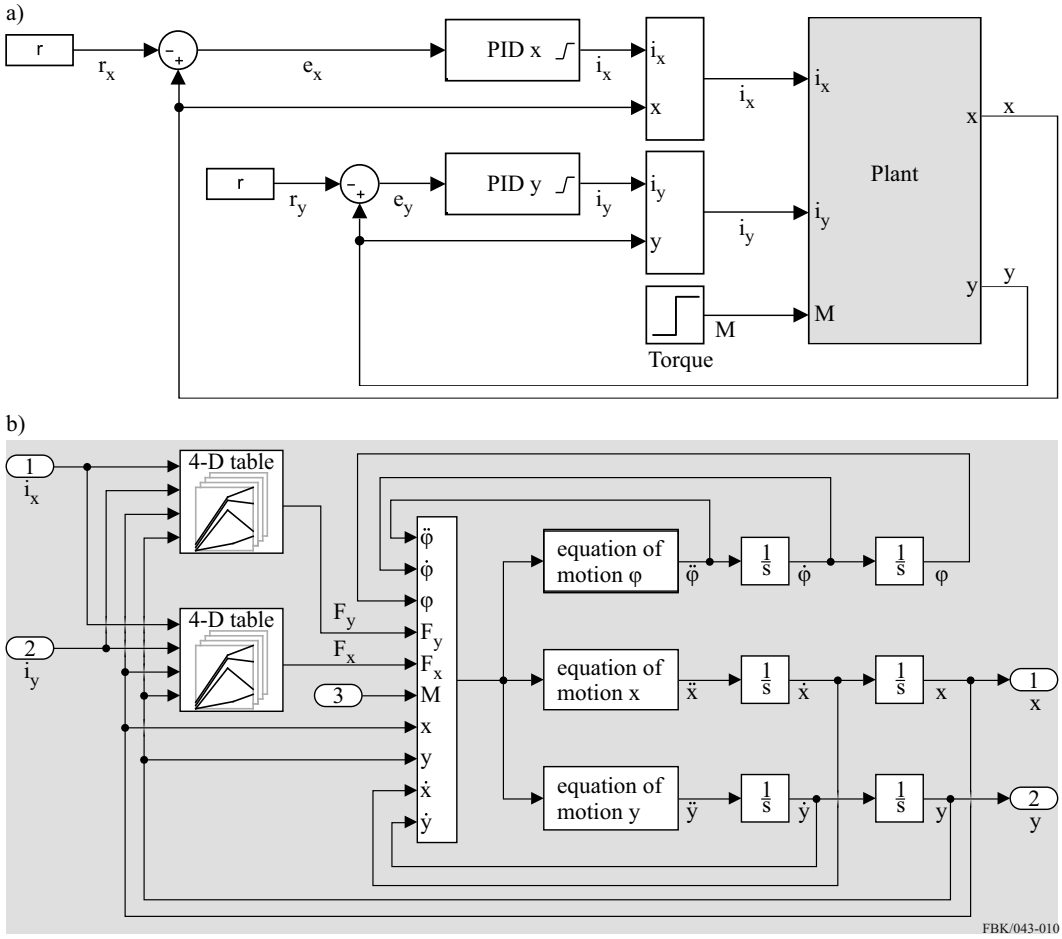

Figure 3 Control system for a spindle rotor supported by two radial heteropolar 4-pole-pair active magnetic bearings.

The model dynamics can be described as follows: During a time step Δt and for a given target position r_x and r_y of the spindle rotor, the PID controllers determine the deviations e_x and e_y from the instantaneous positions x and y and accordingly alter the control currents i_x and i_y. The updated control currents get passed to the plant subsystem (figure 3b)) along with the instantaneous positions x and y of the spindle and the torque of the spindle's driving motor. Within the plant subsystem, the electromagnetic force $f_x, f_y = f(x, y, i_x, i_y)$ is calculated by looking up its x- and y-value corresponding to the instantaneous position and currents within the four-dimensional lookup table. The updated electromagnetic force is then transferred to the rotordynamics model. In order to solve the rotordynamics model, additional data is required. This additional data consists of the instantaneous values of

angular acceleration $\ddot{\varphi}$, angular velocity $\dot{\varphi}$, rotational angle φ, positions x and y and velocities $\dot{x}$ and $\dot{y}$. When all data is evaluated, the rotordynamics model is solved numerically to obtain the accelerations $\ddot{x}$ and $\ddot{y}$. Accelerations are then integrated twice to obtain both updated instantaneous velocities and positions. With the updated positions x and y, the next time step can be computed.

2.2 Process kinematics

The setup of the simulation model for the determination of the process kinematics will be explained with respect to a single-cutting-edge micro end mill with an infinitely sharp cutting edge, as shown in figure 4.

The ideal process kinematics of micro end milling can be modeled by superimposing the translational tool feed movement with a rotational movement of the tool. Without the influence of machine kinematics and a cutting edge radius of zero, the kinematics of a micro milling process with a single-cutting-edge micro end mill can be described by the following equation:

$$\begin{pmatrix} x_P \\ y_P \\ z_P \end{pmatrix} = \begin{pmatrix} r \cdot \sin(\varphi) \\ r \cdot \cos(\varphi) \\ (R-r) \cdot \tan(\chi_r') \end{pmatrix} + \begin{pmatrix} \frac{f_z}{2\pi} \cdot \varphi \\ 0 \\ 0 \end{pmatrix} \quad r \in [0, R] \tag{7}$$

Herein, the tool feed rate of the tool with a radius R is defined by the feed per tooth f_z along the positive x_P-direction. The slope of the cutting edge is reflected by the height function $f(z_P) = (R-r) \cdot \tan(\chi_r')$ along the z_P-direction.

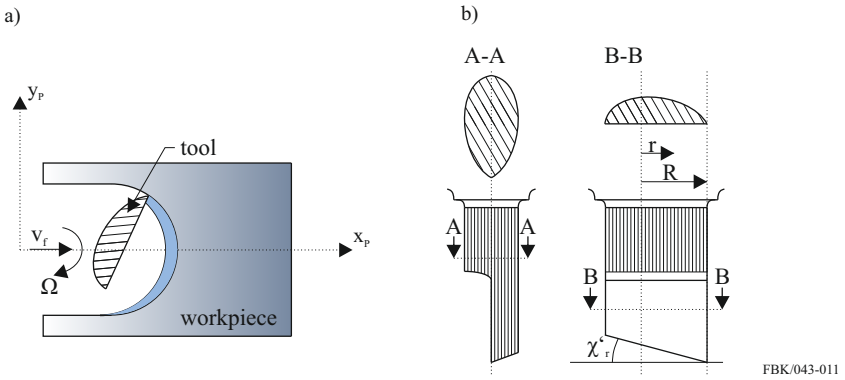

Figure 4 Schematic view of a micro end milling process (a) with a single-cutting-edge tool (b).

2.3 Process-machine-interaction

In the final physical model, the superposition of the machine kinematics and the ideal process kinematics yields the kinematics under consideration of process-machine-interactions. The superposition of the machine and process kinematics is achieved by using the following equation:

$$\begin{pmatrix} x_{PMI} \\ y_{PMI} \\ z_{PMI} \end{pmatrix} = \begin{pmatrix} x_P \\ y_P \\ z_P \end{pmatrix} + \begin{pmatrix} \cos(\varphi) & sin(\varphi) & 0 \\ \sin(\varphi) & -\cos(\varphi) & 0 \\ 0 & 0 & 1 \end{pmatrix} \cdot \begin{pmatrix} x_M \\ y_M \\ z_M \end{pmatrix} \tag{8}$$

This instantaneous position of the tool due to the process kinematics is described by three coordinates x_P, y_P, and z_P, where the P-index stands for process. The position of the tool center point with respect to the machine tool spindle was described by three coordinates x, y, and z in prior sections. For a better understanding, an M-index is added to these coordinates in the following sections, where M stands for machine.

Even though both the process and machine kinematics are modeled using a stationary reference frame, a rotation matrix is required for the correct superposition of both kinematics. The reason for the need of this additional multiplication lies within the nature of the rotordynamics model. Herein, the rotor is not actually spinning but only the physical effects, namely the gyroscopic effect and the rotating damping effect, are taken into account during the formulation of the rotordynamics equation (equation 6). Thus, the actual spin of the tool is accounted for by multiplying the machine kinematics x_m, y_m, and z_m with the rotation matrix about the rotational angle φ.

3 Results

Results will be presented in the following order: First, simulation results of the machine simulation model will be presented. Second, simulation results of the process simulation model and process-machine-interaction will be presented.

3.1 Air bearings

Results in this section will be reported for a single air bearing with the geometry properties and boundary conditions listed in table 1.

Table 1 Geometry properties and boundary conditions used for the analysis.

	parameter	value
geometry	bearing length	$70\,mm$
	rotor diameter	$21\,mm$
	number of orifices	6
	orifice radius	$0.09\,mm$
	bearing gap	$20\,\mu m$
	eccentricity	$3.5\,\mu m$
	perturbation increment	$1\,\mu m$
fluid properties	dynamic viscosity	$18\,\mu Pa \cdot s$
	orifice inlet temperature	$288.15\,K$
	orifice inlet pressure	$6\,bar$
	ambient pressure	$1\,bar$

Using the solution approach presented in section 2.1.1, one obtains the results for the mass flow rate as $\dot{m}_{iterative} = 4.211 \cdot 10^{-5}\,kg/s$. For comparison, the analytically calculated mass flow rate (equation 1) is given as $\dot{m}_{analytic} = 3.433 \cdot 10^{-5}\,kg/s$. Compared to the analytical value, the numerically calculated final value shows an increase of approximately 18.5%. Using the final mass flow rate and derived interface pressure, one can obtain the corresponding stiffness and damping coefficients as described in section 2.1.1.

3.2 Magnetic bearings

Results in this section will be reported for a rotor supported by two heteropolar 4-pole-pair active magnetic bearings. Geometry properties and boundary conditions are listed in table 2.

Table 2 Geometry properties and boundary conditions used for the analysis.

	parameter	value
geometry	rotor mass	$3.6\,kg$
	rotor moment of inertia about z-axis	$7.01 \cdot 10^{-5}\,kg \cdot m^2$
	rotor diameter	$43\,mm$
	iron core diameter	$100\,mm$
	number of poles	8
	number of coil turns per coil	460
	conducting area per coil	$42\,mm^2$
	bearing gap	$0.5\,mm$
bearing properties	bias current	$2.5\,A$
	control current	$\pm 2.5\,A$
	proportional gain	$10,000\,A/m$
	integral gain	$15,000\,A/ms$
	differential gain	$6\,As/m$
additional properties	simulation time	$4\,s$
	step size	$1 \cdot 10^{-4}\,s$
	solver	ode3
	target position in x_M- and x_M-direction	$0\,mm$

The control system model (figure 3) is used to simulate the time-dependent vibrations of the rotor. Figure 5 shows the corresponding vibration amplitudes, angular velocity and driving torque. During the simulation time of $4\,s$, the rotor's motion can be divided into three stages.

The first stage is labeled the lift-off phase in figure 5, ranging from $0\,s$ to $1\,s$. During this phase, the rotor is brought into levitation. During this stage, no driving torque is applied to the rotor and thus the rotor does not rotate. As can be seen in figure 5, the rotor is brought up from its initial resting position at approximately $3.5 \cdot 10^{-4}\,m$ to its target position of $x_{M,target} = y_{M,target} = 0\,m$. With the PID controller values of table 2, a maximum overshoot of approximately 23% is observed, followed by additional smaller oscillations until the rotor approaches its target position with an almost constant negative incline.

The second phase is labeled the acceleration phase. During this phase, a constant driving torque of $2\,Nm$ is applied to the rotor, generating a constant slope of the angular velocity up until $4000\,rad/s$ $(38,200\,min^{-1})$.

The third stage is labeled the stationary phase. Once the rotor has reached its nominal speed of $4,000\,rad/s$ no more driving torque is applied, leading to a constant rotor speed. In this phase, in addition to the mass unbalance, cutting forces are applied on the tool tip and applied once the simulation time reached $3\,s$.

The magnitude of the cutting force f_{cut} was set equal to $1\,N$, based on experimental investigations with comparable process parameters [16]. For a single-cutting-edge micro end mill, the cutting force can be assumed as a harmonic force with an excitation frequency ν equal to the angular velocity $\dot{\varphi}$. Since no influence of changing cutting conditions is considered (such as depth of cut being lower than the minimum chip thickness), the cutting force was superimposed with an additional random white noise f_{noise} to introduce random changes in the cutting force.

The shift of $1\,s$ between the rotor reaching its nominal speed and the application of cutting forces was implemented in order for remaining oscillations of the acceleration phase to subside. Figure 5 shows that the magnetic bearings are able to stabilize the rotor despite the excitation by mass unbalance and cutting forces.

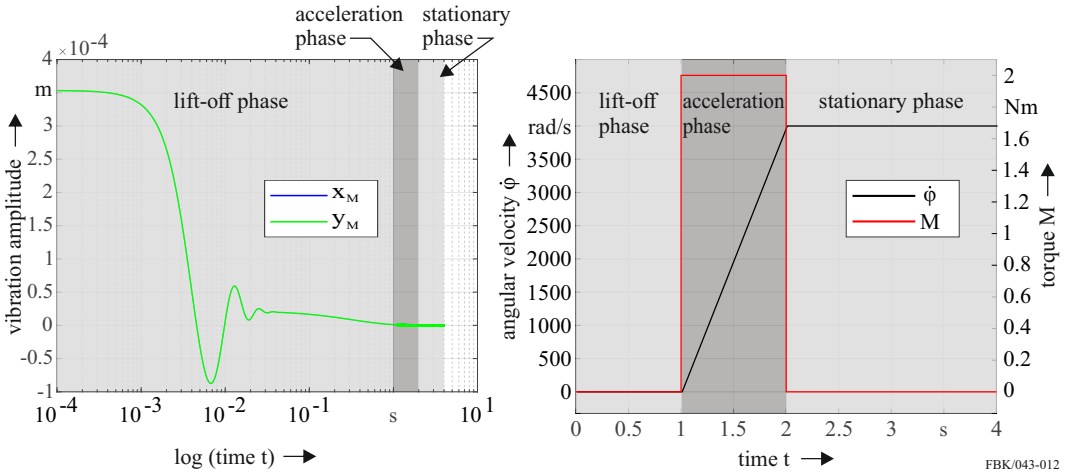

Figure 5 Vibration amplitudes, angular velocity and driving torque for a rotor supported by two radial heteropolar 4-pole-pair active magnetic bearings.

3.3 Process-machine-interaction

Ideal process kinematics results in this section will be shown for the process parameters listed in table 3. Process-machine-interaction results will be shown for the same process parameters under consideration of the machine kinematics determined by the physical model of the magnetic bearing spindle (see section 3.2).

Table 3 Process parameters used for the analysis.

parameter	value
effective tool radius	$25\,\mu m$
feed per tooth	$4\,\mu m$
cutting depth	$2.1\,\mu m$
minor cutting edge angle	$12°$
rotational speed	$38,200\,min^{-1}$

Using the process parameters listed in table 3, one can obtain the tool tip path trajectory in x_P-direction, y_P-direction, and x_P-y_P-direction for ideal process kinematics (no process-machine-interactions) and under consideration of process-machine-interactions as a function of time or absolute angular tool position as shown in figure 6. Figure 6a) and c) show the $x_P(t)$- and $y_P(t)$-trajectories of the tool tip (radius of $R = 25\,\mu m$) without the consideration of process-machine-interactions. As can be seen, the rotational movement of the tool tip leads to a sinusoidal tool path trajectory. Since the tool feed movement is modeled along the x_P-direction, the absolute amplitude of the sinusoidal tool path trajectory in x_P-direction is steadily rising due to the applied tool feed rate. In figure 6b), d), and f), the ideal process kinematics are superpositioned with the machine kinematics as described in section 2.3.

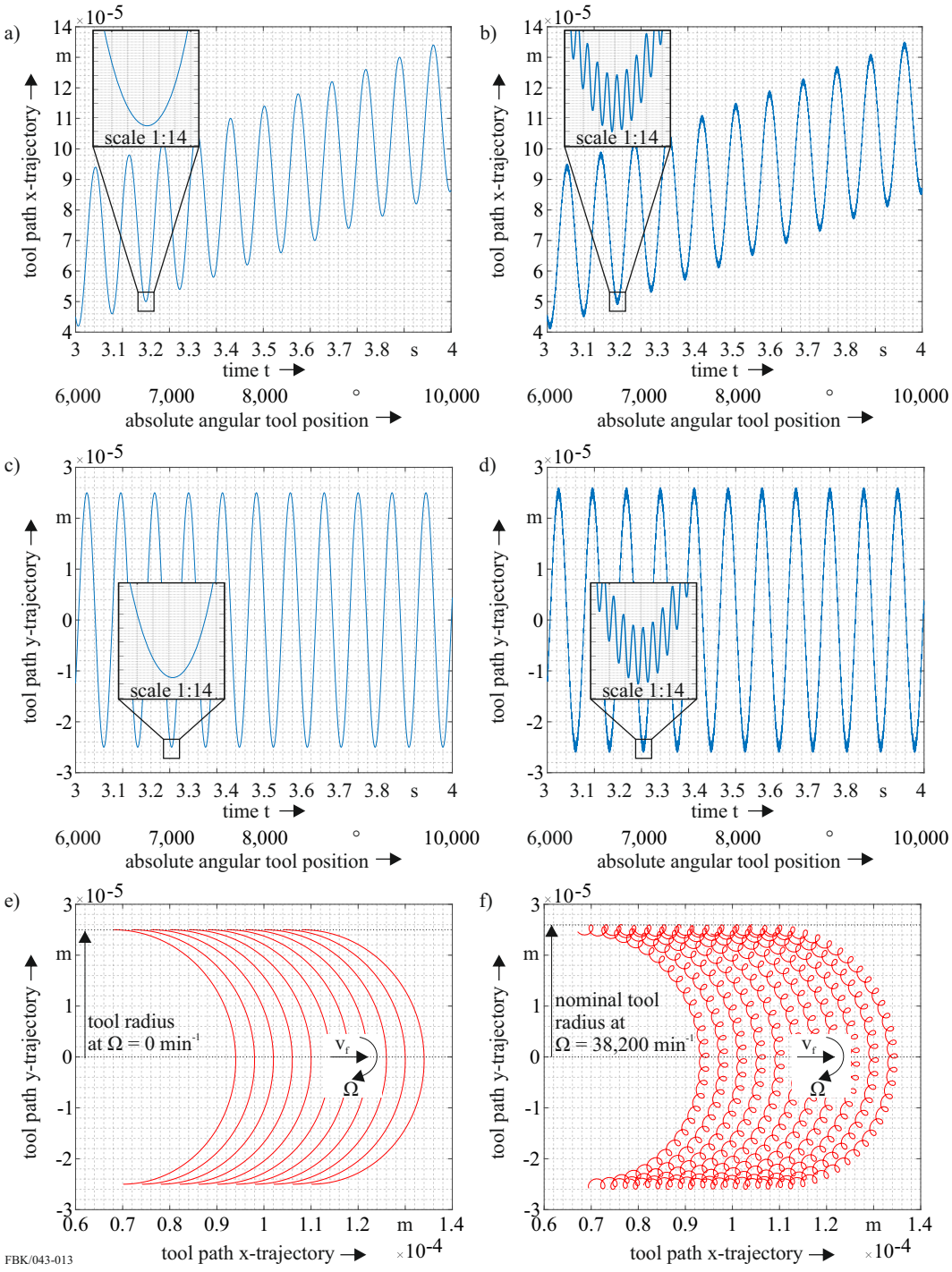

Figure 6 Tool tip path trajectory in x_P-direction, y_P-direction and x_P-y_P-direction for ideal process kinematics (a), c), e)) and under consideration of process-machine-interactions (b), d), f)).

Comparing the trajectories with and without process-machine-interactions against each other, it can be noted that the tool path trajectory under consideration of process-machine-interactions exhibits the same overall behavior as the ideal tool path trajectory but shows additional continuous high-frequency-oscillations with a small amplitude overlapping the ideal tool path trajectory.

Plotting the tool path trajectories in x_P- and y_P-direction (figure 6a) and c)) and figure 6b) and d) respectively) against each other gives the graphs depicted in figure 6e) and f). It must be noted that in these figures, only the front cutting motion is shown.

The aforementioned high-frequency-oscillations can be seen in figure 6f) in terms of loops which superimpose the ideal movement of the tool. In figure 6e), the ideal tool radius equals $R = 25\,\mu m$, whereas figure 6f) shows the nominal tool radius at a rotational speed of $38,200\,min^{-1}$. This nominal tool radius equals approximately $R_{nominal} = 27\,\mu m$, showing that the process conditions, in this case cutting width, do change under consideration of machine kinematics.

A three-dimensional surface representation and the surface profile of the ideal and process-machine-interaction-considering tool path trajectory is presented in figure 7. Unlike figure 6, the surface plots in 7a) and b) depict the trajectory of the whole tool, not just the tool tip. Further, visualizing the tool path trajectory along the z_P-axis picks up on equation 7, showing the effects of the height function $f(z_P)$ used to model the cutting edge.

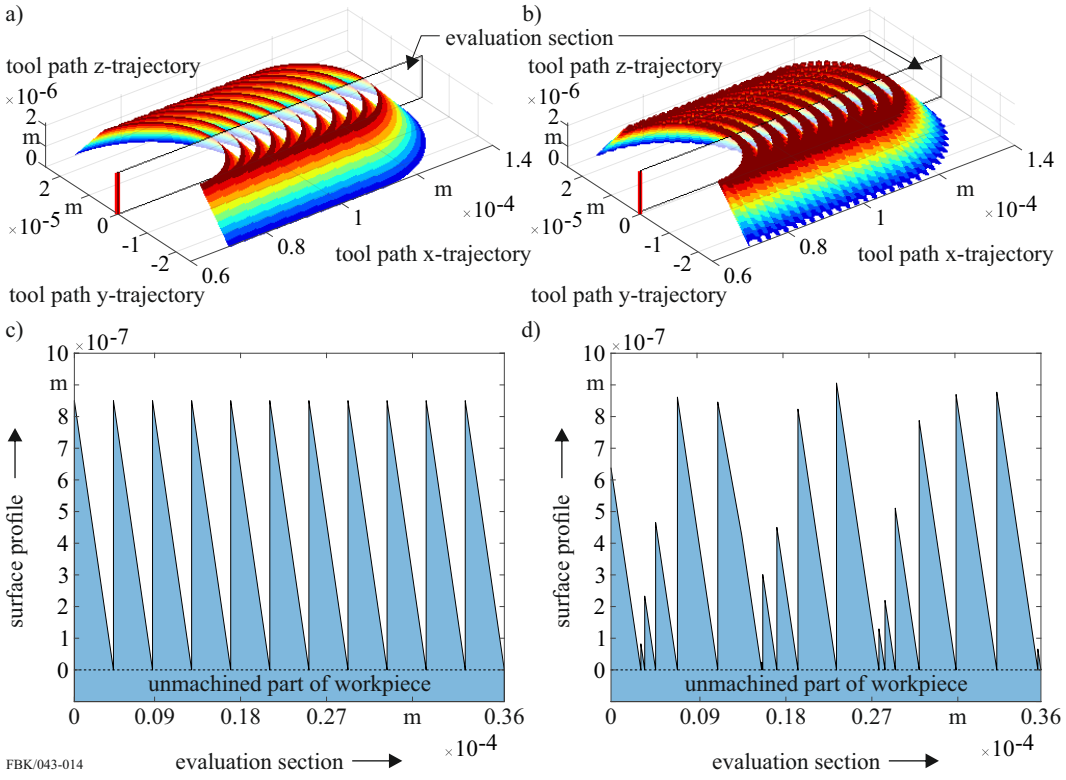

Figure 7 Three-dimensional view of tool path trajectory and filtered workpiece surface profile visualization for ideal process kinematics (a), c)) and under consideration of process-machine-interactions (b), d)).

Figure 7a) and b) also shows a graphical representation of the slicing plane used for the evaluation of the surface profile and roughness. The evaluation section of the surface profile visualizations in figure 7c) and d) is based on this slicing plane.

The unfiltered surface profile is filtered by evaluating the incline between all consecutive data points and comparing these inclines to the height function $f(z_P)$ of the minor cutting edge (see section 2.2 and equation 7). Excluded from this filtering are those data points that immediately follow the maximum values, since these data points form a vertical line that represents the vertical tool flank (see figure 4).

The filtered surface profile without and with consideration of process-machine-interactions is shown in figure 7c) and d). Regarding the surface profile without consideration of process-machine-interactions (figure 7c)), the graph shows a surface profile with equidistant and equal local minimum and maximum values as well as constant inclines between all local minima and maxima. The maximum surface roughness value equals $0.850\,\mu m$, and thus only about 40% of the cutting depth. The R_a-value is calculated by integrating the area between the surface roughness and the x_P-axis and equals $0.425\,\mu m$.

Regarding the surface profile with consideration of process-machine-interactions (figure 7d)), the surface profile exhibits big differences compared to the surface profile in 7c). As such, the local minima and maxima are neither equidistant nor equal anymore. The maximum surface roughness value equals $0.906\,\mu m$ and thus is 6% higher than the maximum surface roughness value without consideration of process-machine-interactions. Further, the R_a-value slightly increases to a value of $0.460\,\mu m$.

4 Discussion

This section discusses the presented methods and results in terms of application possibilities and compares them against other published work.

4.1 Air bearings

The presented model for the physical modeling of the pressure distribution of aerostatic journal bearings differs from existing models in multiple ways.

The implementation of the orifice region (I) into the physical model allows to develop a deeper understanding of the interactions between orifice region and entrance region, as was stated as an objective for future air bearing designs in [11].

The use of the coupled model omits the need to guess or approximate a discharge coefficient as was done in [29, 18]. Herein, the discharge coefficient was computed for an aerostatic thrust pad with a single orifice in the middle of the pad. The presented model uses the actual geometry of the radial bearing, including the orifice positions and surface curvature of both the rotor and the stator. Comparing the mass flow rate used in various approaches [29, 18] against the numerically calculated value using the presented method, it becomes clear that the consideration of the actual radial bearing geometry and configuration influences the mass flow rate (18.5% in the presented results), which will eventually influence the simulation of the process-machine-interactions.

The use of the Reynolds-averaged Navier-Stokes equations instead of the Reynolds equation offers the possibility to include inertia effects, turbulence and flow velocity and direction effects. Specifically, this enables the determination of the pressure distribution of aerostatic bearings featuring angled injection orifices similar to the physical model presented in [32]. However, with the model presented in this paper, the dynamic damping coefficients can be calculated, which eventually allows for a more accurate rotordynamics model of air bearing spindles, providing a way for the investigation into new and improved air bearing designs for air bearing spindles, such as bearings with angled injection orifices.

Drawbacks of the use of the Reynolds-averaged Navier-Stokes equations instead of the Reynolds equation are the increase in required computer resources, an increase in modeling time as well as an increased time consumption to compute the pressure distribution and the dynamic characteristics. Further, the presented method exhibits a lower robustness, which can lead to convergence difficulties.

4.2 Magnetic bearing spindles

Using a finite element model for the evaluation of the electromagnetic forces instead of the magnetic circuit method has the following advantages:

Nonlinear behavior such as magnetic saturation can be incorporated into the analysis, which is not possible using the magnetic circuit method.

No approximation of the electromagnetic forces using analytical formulas is required, leading to an overall more accurate close loop model and eventually to a more accurate model of the process-machine-interactions.

Implementing the numerically evaluated electromagnetic forces through lookup tables in the close loop model offers the possibility to include accurate properties of the magnetic bearings while keeping simulation time (and thus controller design and optimization time) as small as possible since no finite element analysis must be employed during each time step.

It is important to also mention the limits of the presented model.

Suitable lookup table data points have to be chosen in order to generate a reliable lookup table.

Every single lookup table data point has to be generated using the finite element model, which is more time consuming than using analytical formulas.

With respect to the time consumption of the finite element model to solve all necessary data points used for the presented results in section 3.2, the authors' assumption is that for greater number of inputs (> 4) as well as greater ranges of inputs (> 15 values to represent the behavior of every single input) the presented approach is not feasible anymore.

4.3 Process-machine-interaction

The presented approach for the physical modeling of process-machine-interactions offers a feasible approach to analyze process-machine-interactions in micro manufacturing. Combining a purely kinematic mathematical model of the ideal process kinematics with a rotordynamics model of the machine tool spindle under consideration of the cutting forces offers the possibility to capture the influence of the cutting forces on the machine‘s motion as well as the influence of the machine´s motion on the tool path trajectory.

Compared against several existing approaches, the presented approach offers several advantages.

The rotordynamics model is set up in a modular way. This allows for a straight-forward implementation of additional relevant aspects that influence the machine tool spindle‘s behavior (see section 2.1) and were not yet included in the analyses presented in section 3.

Even though the ideal process kinematics are modeled using a purely kinematic approach similar to approaches in [3, 23], cutting forces can be included within the rotordynamics model of the machine simulation model, providing a suitable approach to model process-machine-interactions.

The modular setup of both the machine and process models offers great flexibility. As such, instead of the micro end milling process analyzed in this paper (section 2.2), the process simulation model can be adapted to represent other processes, such as micro grinding [23]. Similarly, the machine simulation model can be adapted by changing the rotor and/or tool geometry to represent other machines and/or tools, such as micro grinding pencil tools [4].

However, the presented approach is limited. Cutting forces must be acquired through experimental investigations or by conducting micro cutting simulations. However, care must be taken regarding the implementation of these cutting forces in the presented model:

- Measured cutting forces already include the process-machine-interactions of the employed machine tool and cutting process. Hence, using these forces as an input for the cutting forces to investigate process-machine-interactions is not appropriate.
- Using micro cutting simulations requires precise knowledge of the material parameters of the workpiece and suitable constitutive laws [2]. Further, micro cutting simulations are rather time consuming [25].

Since the process kinematics are modeled using a purely kinematic approach and the machine kinematics only include a simple representation of cutting forces, no elasticity and/or plasticity of the workpiece is considered. Effects, such as ploughing and burr formation, hence cannot be examined.

5 Conclusion and outlook

This paper presented methods for the physical modeling of process-machine-interactions in micro manufacturing. For this purpose, both the process and the machine kinematics were modeled separately and then superimposed. In particular, methods to model air bearing and magnetic bearing spindles were investigated as part of the machine simulation model and micro end milling was investigated as part of the process simulation model.

Machine kinematics were determined by using a fluid dynamics model for the air bearings, an electromagnetic model for the magnetic bearings, and a rotordynamics model for the machine tool spindle rotor. Process kinematics were modeled using a purely kinematic approach. Incorporation of cutting forces was implemented by applying them as an excitation in the rotordynamics model. Finally, process-machine-interactions were modeled by superimposing the machine kinematics and process kinematics under consideration of the kinematic relationship between both components.

The following conclusions can be drawn from this analysis:

- The presented physical model for air bearings is well suited for a broad range of air bearing applications, allowing for new and improved bearing designs while yielding results with higher accuracy compared to existing modeling approaches. Possible applications include the analysis of air bearings with angled injection orifices, the investigation into effects of manufacturing errors on bearing performance, and spherical air bearings;
- Modeling the force-current-displacement relationship $f_x, f_y = f(x, y, i_x, i_y)$ of magnetic bearings with a finite element electromagnetic model and implementing this relationship by means of lookup tables in a control system model provides greater modeling accuracy than using the magnetic circuit method, while keeping computing time acceptable for a moderate number of inputs. This also allows the development of more sophisticated controllers for magnetic bearings. Application possibilities include conducting new analyses of homopolar bearings [17], more aggressive bearing designs in terms of geometry and operating configurations, and spherical magnetic bearings;
- Splitting up the process-machine-interactions simulation model during setup into a physical model of the machine (under consideration of the cutting forces) and a kinematic model of the process provides a feasible method for the simulation-based investigation of process-machine-interactions in micro manufacturing.

Currently, the presented simulations models are being validated to confirm their suitability for the prediction of process-machine-interactions including the surface profile and surface roughness values. In future works, the rotordynamics model will be extended to include a detailed three-dimensional representation of the tool flexibility. Advanced process models will be set up and replace the simple representation of the cutting forces. These process

models may be based on chip formation simulations and can extend the suitability of the physical model to investigate process-machine-interactions in micro end milling by including elasticity and plasticity effects of the workpiece as well as a more accurate representation of the cutting forces. Further, sensitivity studies will be conducted to investigate effects of upstream simulation results on the final tool path and surface roughness results.

References

1 Shukri M. Afazov, Svetan M. Ratchev, Joel Segal, and Atanas A. Popov. Chatter modelling in micro-milling by considering process nonlinearities. *International Journal of Machine Tools and Manufacture*, 56:28–38, 2012. doi:10.1016/j.ijmachtools.2011.12.010.

2 Ravi S. Anand and Karali Patra. Modeling and simulation of mechanical micro-machining—a review. *Machining Science and Technology*, 18(3):323–347, 2014. doi:10.1080/10910344.2014.925377.

3 Jan C. Aurich, Martin Bohley, Ingo G. Reichenbach, and Benjamin Kirsch. Surface quality in micro milling: Influences of spindle and cutting parameters. *CIRP Annals*, 66(1):101–104, 2017. doi:10.1016/j.cirp.2017.04.029.

4 Jan C. Aurich, Marina Carrella, and Michael Walk. Micro grinding with ultra small micro pencil grinding tools using an integrated machine tool. *CIRP Annals*, 64(1):325–328, 2015. doi:10.1016/j.cirp.2015.04.011.

5 George K. Batchelor. *An Introduction to Fluid Dynamics*. Cambridge Mathematical Library. Cambridge University Press, 2000. doi:10.1017/CBO9780511800955.

6 Richard Bellman. Perturbation techniques in mathematics, physics and engineering (holt, rinehart and winston, london, 1964), 118 pp., 30s. *Proceedings of the Edinburgh Mathematical Society*, 14(4), 1965. doi:10.1017/S0013091500009068.

7 Christian Brecher, Martin Esser, and Stephan Witt. Interaction of manufacturing process and machine tool. *CIRP Annals*, 58(2):588–607, 2009. doi:10.1016/j.cirp.2009.09.005.

8 Berend Denkena and Ferdinand Hollmann. *Process Machine Interactions*. Springer Berlin Heidelberg, Berlin, Heidelberg, 2012. doi:10.1007/978-3-642-32448-2.

9 Mohamed E. Eleshaky. Cfd investigation of pressure depressions in aerostatic circular thrust bearings. *Tribology International*, 42(7):1108–1117, 2009. doi:10.1016/j.triboint.2009.03.011.

10 Michael I. Friswell, John E. T. Penny, Seamus D. Garvey, and Arthur W. Lees. *Dynamics of Rotating Machines*. Cambridge Aerospace Series. Cambridge University Press, 2010. doi:10.1017/CBO9780511780509.

11 Qiang Gao, Wanqun Chen, Lihua Lu, Dehong Huo, and Kai Cheng. Aerostatic bearings design and analysis with the application to precision engineering: State-of-the-art and future perspectives. *Tribology International*, 135:1–17, 2019. doi:10.1016/j.triboint.2019.02.020.

12 Siyu Gao, Kai Cheng, Hui Ding, and Hongya Fu. Multiphysics-based design and analysis of the high-speed aerostatic spindle with application to micro-milling. *Proceedings of the Institution of Mechanical Engineers, Part J: Journal of Engineering Tribology*, 230(7):852–871, 2016. doi:10.1177/1350650115619609.

13 Ichiro Inasaki, Bernhard Karpuschewski, and Hwasoo Lee. Grinding chatter–origin and suppression. *CIRP Annals*, 50(2):515–534, 2001. doi:10.1016/S0007-8506(07)62992-8.

14 John D. Jackson. *Classical electrodynamics*. John Wiley & Sons, 3rd edition, 1999.

15 Martin B. G. Jun, Xinyu Liu, Richard E. DeVor, and Shiv G. Kapoor. Investigation of the dynamics of microend milling—part i: model development. *Journal of Manufacturing Science and Engineering*, 128(4):893–900, 2006. doi:10.1115/1.2193546.

16 Sonja Kieren-Ehses, Martin Bohley, Tobias Mayer, Benjamin Kirsch, and Jan C. Aurich. Effect of high spindle speeds on micro end milling of commercially pure titanium. *Proceedings of the 20th euspen International Conference*, pages 61–62, 2020.

17 Eric H. Maslen and Gerhard Schweitzer. *Magnetic Bearings: Theory, Design, and Application to Rotating Machinery*. Springer-Verlag Berlin Heidelberg, 2009. doi:10.1007/978-3-642-00497-1.

18 Christopher Müller, Sebastian Greco, Benjamin Kirsch, and Jan C. Aurich. A finite element analysis of air bearings applied in compact air bearing spindles. *Procedia CIRP - 16th CIRP Conference on Modelling of Machining Operations*, 58:607–612, 2017. doi:10.1016/j.procir.2017.03.337.

19 Christopher Müller, Benjamin Kirsch, and Jan C. Aurich. Compact air bearing spindles for desktop sized machine tools. *Small Machine Tools for Small Workpieces*, 55:21–34, 2017. doi:10.1007/978-3-319-49269-8_2.

20 Tej Pratap, Karali Patra, and Alexander A. Dyakonov. Modeling cutting force in micro-milling of ti-6al-4 v titanium alloy. *Procedia Engineering*, 129:134–139, 2015. doi:10.1016/j.proeng.2015.12.021.

21 Ingo G. Reichenbach. *Beitrag zur Beherrschung der Mikrofräsbearbeitung von Polymethylmethacrylat*. Dissertation, Technische Universität Kaiserslautern, 2017.

22 Pablo Rodríguez and Julio E. Labarga. A new model for the prediction of cutting forces in micro-end-milling operations. *Journal of Materials Processing Technology*, 213(2):261–268, 2013. doi:10.1016/j.jmatprotec.2012.09.009.

23 Dinesh Setti, Peter A Arrabiyeh, Benjamin Kirsch, Marius Heintz, and Jan C Aurich. Analytical and experimental investigations on the mechanisms of surface generation in micro grinding. *International Journal of Machine Tools and Manufacture*, 149:103489, 2020. doi:10.1016/j.ijmachtools.2019.103489.

24 Andras Z. Szeri. *Fluid film lubrication*. Cambridge university press, 2010. doi:10.1017/CBO9780511782022.

25 Thanongsak Thepsonthi and Tuğrul Özel. 3-d finite element process simulation of micro-end milling ti-6al-4v titanium alloy: experimental validations on chip flow and tool wear. *Journal of Materials Processing Technology*, 221:128–145, 2015. doi:10.1016/j.jmatprotec.2015.02.019.

26 Eckart Uhlmann, F Mahr, Y Shi, and U von Wagner. Process machine interactions in micro milling. In *Process Machine Interactions*, pages 265–284. Springer, 2013. doi:10.1007/978-3-642-32448-2_12.

27 Frank Vollertsen, Dirk Biermann, Hans N. Hansen, I. S. Jawahir, and Karl Kuzman. Size effects in manufacturing of metallic components. *CIRP Annals*, 58(2):566–587, 2009. doi:10.1016/j.cirp.2009.09.002.

28 Frank Wardle. *Ultra precision bearings*. Woodhead Publishing, Cambridge, 2015.

29 Tobias Waumans. *On the design of high-speed miniature air bearings: Dynamic stability, optimisation and experimental validation*. Dissertation, Katholike Universiteit Leuven, 2009.

30 David C. Wilcox. *Turbulence modeling for CFD*, volume 2. DCW industries La Canada, CA, 1998.

31 Jens P. Wulfsberg and Adam Sanders. *Small Machine Tools for Small Workpieces: Final Report of the DFG Priority Program 1476*. Lecture Notes in Production Engineering. Springer International Publishing, 2017. doi:10.1007/978-3-319-49269-8.

32 He Chun Yu, Wen Qi Ma, Zu Wen Wang, and Li Fang Xu. Cfd research on aerostatic bearing with tangential supply holes. *Advanced Materials Research*, 97:2021–2026, 2010. doi:10.4028/www.scientific.net/AMR.97-101.2021.